Available online at www.sciencedirect.com
ScienceDirect
Journal of Computational Physics 225 (2007) 554–567
JOURNAL OF COMPUTATIONAL PHYSICS
www.elsevier.com/locate/jcp

A rescaling scheme with application to the long-time simulation of viscous fingering in a Hele–Shaw cell

Shuwang Li [a], John S. Lowengrub [a,*], Perry H. Leo [b]

[a] Department of Mathematics, University of California at Irvine, Irvine, CA 92697, USA
[b] Department of Aerospace Engineering and Mechanics, University of Minnesota, Minneapolis, MN 55455, USA

Received 4 August 2006; received in revised form 17 December 2006; accepted 18 December 2006
Available online 13 January 2007

Abstract

In this paper, we present a time and space rescaling scheme for the computation of moving interface problems. The idea is to map time–space such that the interfaces can evolve exponentially fast in the new time scale while the area/volume enclosed by the interface remains unchanged. The rescaling scheme significantly reduces the computation time (especially for slow growth), and enables one to accurately simulate the very long-time dynamics of moving interfaces. We then implement this scheme in a Hele–Shaw problem, examine the dynamics for a number of different injection fluxes, and present the largest and most pronounced viscous fingering simulations to date.

Keywords: Hele–Shaw; Saffman–Taylor instability; Boundary integral method; Moving boundary problems; Fractal; Self-similar

1. Introduction

Many physical problems involve moving interfaces, such as the growth of crystals, the dynamics of Hele–Shaw flows, etc. Characterizing the formation and dynamics of complex interface morphologies due to instability has long been a challenging research topic (e.g. [1–6]). While numerical simulation has become one of the most important tools for investigating the motion of interfaces, it is still difficult to obtain accurate approximations, especially for the long-time evolution of interfaces. Specifically, difficulties arise because one must efficiently and accurately resolve the multiple time and space scales involved in the physics that lead to the development of complex morphologies.

There are many computational methods that have been developed for simulating interfacial instabilities, such as boundary integral methods (e.g. see [7,8,33]), the level set methods (e.g. see [10–13]), volume of fluid methods (e.g. see [14,15]), front-tracking methods (e.g. see [16,17]), immersed interface methods (e.g. see [18,19]), phase field methods (e.g. see [20–23]) as well as hybrid methods (e.g. see [24–27]). These methods are usually coupled with adaptive mesh algorithms to gain more efficiency. When applicable (e.g. for piecewise

* Corresponding author. Tel.: +1 949 824 2655; fax: +1 949 824 7993.
E-mail addresses: lis@math.uci.edu (S. Li), lowengrb@math.uci.edu (J.S. Lowengrub), phleo@aem.umn.edu (P.H. Leo).

0021-9991/$ - see front matter
doi:10.1016/j.jcp.2006.12.023

homogeneous problems) boundary integral methods are typically the most accurate methods for simulating interface motion because the dimensionality of the problem is reduced by one and there are well-developed accurate and stable discretizations of boundary integral equations. Further, while boundary integral methods are important in their own right, they can also serve as benchmarks for other more general methods.

A decade ago, Hou, Lowengrub and Shelley (HLS94) significantly advanced the state-of-the-art of boundary integral methods in a study of viscous fingering (the Saffman–Taylor instability) in a Hele–Shaw cell [9], as well as studies of the motion of vortex sheets with surface tension [28]. The algorithm relied on an analysis of the equations at small spatial scales (SSD [9]) that identified and removed the source of stiffness introduced by surface tension. This enabled the use of large time steps and made long-time simulations possible. To further enhance the efficiency of the algorithm, the fast multipole method [41] was used to evaluate the boundary integrals. Later on, this method was successfully adapted to other physical problems such as microstructural evolution in inhomogeneous elastic domains [34], solid tumor growth [35], crystal growth [36–38], etc. The resulting body of research has led to many interesting discoveries (e.g. see [29–32] and the review article [33]).

Very recently, Fast and Shelley [39] re-ran the long-time simulation of a Hele–Shaw bubble originally presented in [9]. By comparing the CPU time with that used in [9], Moore's law was verified: the computation power has increased a hundredfold since 1994. For example, it took only 14 h to reproduce the bubble simulation in [9], roughly 1% of the 50 days required in 1994. Using the same wall time (50 days), Fast and Shelley ran the simulation 10 times longer and computed an interface using up to $N = 32{,}768$ mesh points. The bubble assumes a complex fingering pattern and is about 4 times larger (in radius) than the one presented in [9]. By computing farther in time, Fast and Shelley identified the emergence of a new scaling regime in the relationship between the area $A(t)$ and the arclength $L(t)$, which reflects the highly ramified bubble structure.

Complex viscous fingering patterns reflect the Saffman–Taylor instability [5], which occurs when the stabilizing forces (e.g. surface tension) and the destabilizing driving force (e.g. flux or flow injection rate) are not balanced. For example, in [9,39], a constant flux (constant air injection rate) was used. As suggested by the linear stability analysis, as the bubble grows, larger and larger wavenumbers become unstable, which leads to the nonlinear development of a ramified pattern by repeated tip-splitting. Moreover, for a constant flux, the equivalent bubble radius evolves as $\mathrm{d}R/\mathrm{d}t \sim R^{-1}$, where R is the radius of a circle with the same area as the bubble. Consequently the velocity of the bubble, $\mathrm{d}R/\mathrm{d}t$, decreases as R increases (the bubble grows). From the perspective of numerical computation, this makes the problem highly challenging. Not only does the complex fingering pattern require many mesh points to resolve the interface, but also the intrinsic slow growth (e.g. due to an applied constant injection flux) makes simulations of the evolution to large sized bubbles very expensive.

In this paper, we develop a rescaling scheme which enables one to accurately simulate the long-time dynamics of moving interfaces. In this approach, time is scaled such that the bubble size grows exponentially fast in new time scale, and space is scaled such that the area is constant in the new frame. In the numerical scheme, an analytical formula is used to determine the overall growth due to flux and is therefore free of discretization error. The scheme overcomes the intrinsic slow growth mechanism while maintaining the original physics. Note that very recently we used a specific form of the rescaling scheme to simulate the very long-time dynamics of compact crystals under specialized growth conditions [37,38]. Here, we present a more general version of the scaling scheme, and demonstrate the utility of the scheme in accurately simulating highly ramified Hele–Shaw bubbles over a range of injection fluxes.

By reducing the computation time, this rescaling scheme significantly improves the performance of the boundary integral method originally developed by Hou et al. [9]. In fact, only minor changes to the original algorithm are needed. Using a computer with CPU 2.2 GHz Pentium 4 running Linux (similar to the one used by Fast and Shelley in [39]), we can simulate a high resolution bubble in 6 days that took 50 days for Fast and Shelley [39] to compute. We then continue the simulation significantly longer in time and identify another transition in scaling.

We also investigate the long-time interface morphologies under several injection fluxes $J \propto R(t)^p$ with $p = 1$, 0 and -1, examine the morphologies and measure the bubble complexity in terms of a relation between area $A(t)$ and arclength $L(t)$, i.e. $A(t) \sim L(t)^\gamma$. The relation reflects the underlying physics: when $\gamma < 2$, the destabilizing driving force (flux) dominates the evolution and leads to ramified (e.g. fractal-like) shapes, the smaller the power, the more complex the shape; when $\gamma = 2$, the stabilizing force (surface tension) and destabilizing

factor balance, and leads to the development of compact morphologies. For example, when $J \propto R$, the interface rapidly evolves into a highly ramified fingering pattern and $\gamma \approx 1$ at long times; when $J \propto 1$, the interface also develops a ramified fingering pattern and $\gamma \approx 1.5$ at long times. When $J \propto 1/R$, shape perturbations grows rapidly at early times, however, at long times nonlinear stabilization occurs and leads to the existence of noncircular limiting shapes, i.e. the morphologies of a growing bubble tend to noncircular limiting shapes that evolve self-similarly and $\gamma \approx 2$. In this regime, the time scales for growth and surface tension stabilization balance. A similar phenomenon is observed in crystal growth [37,38].

This paper is organized as follows: in Section 2, we review the governing equations for an exterior moving interface problem (e.g. Hele–Shaw flow); in Section 3, we present the rescaling scheme; in Section 4, we discuss numerical results; and in Section 5, we give conclusions.

2. Governing equations

2.1. Boundary integral formulation

Many important problems are governed by Laplace's equation in a moving domain (e.g. quasi-steady crystal growth, Hele–Shaw bubbles, etc.). Using potential theory, the solutions can be written in terms of boundary integrals thereby reducing dimensionality by 1. For the sake of brevity, we focus our study on the following exterior moving interface problem and its application to Hele–Shaw bubbles. Let E be an open region in the plane exterior to a closed interface $\Sigma(t)$, which we assume to be smooth. The exterior Dirichlet problem is

$$\Delta u(\mathbf{x}) = 0 \quad \text{for } \mathbf{x} \in E, \tag{1}$$

where the harmonic function $u(\mathbf{x})$ represents the pressure in the Hele–Shaw problem (or temperature in quasi-steady crystal growth). The boundary condition is

$$u(\mathbf{x}) = f(\mathbf{x}) \quad \text{for } \mathbf{x} \in \Sigma(t), \tag{2}$$

where $f(\mathbf{x})$ is proportional to the curvature of the interface in the problems listed above. For simplicity, we consider an injection flux $J(t)$ supplied at the origin

$$\int_{\Sigma_0} \frac{\partial u}{\partial \mathbf{n}} \, \mathrm{d}s = J(t), \tag{3}$$

where Σ_0 is a small circle centered at origin. The interface evolves as

$$V(\mathbf{x}) = \mathbf{n} \cdot \frac{\mathrm{d}\mathbf{x}}{\mathrm{d}t} \quad \text{for } \mathbf{x} \in \Sigma, \tag{4}$$

where V is the normal velocity of the interface (e.g. $V = -\nabla u|_{\Sigma} \cdot \mathbf{n}$ for the Hele–Shaw problem), and $\mathbf{n}$ is the normal at point $\mathbf{x} \in \Sigma(t)$ pointing into E. Note that flux J is the integral flux and specifies the time derivative of the area that the interface $\Sigma(t)$ encloses.

We reformulate Eqs. (1), and (3) as a boundary integral equation where we represent the field $u(\mathbf{x})$ through a double-layer potential. As suggested by Mikhlin [40], in two dimensions, we seek a solution in the form,

$$u(\mathbf{x}) = \frac{1}{2\pi} \int_{\Sigma(t)} \mu(\mathbf{x}') \left[\frac{\partial \ln |\mathbf{x} - \mathbf{x}'|}{\partial \mathbf{n}(\mathbf{x}')} + 1 \right] \mathrm{d}s(\mathbf{x}') + J \ln |\mathbf{x}|, \tag{5}$$

where $\mu(\mathbf{x})$ is the dipole density on $\Sigma(t)$. Using the boundary condition given by Eq. (2), μ can be calculated by solving a 2nd kind Fredholm integral equation,

$$\mu(\mathbf{x}) - \frac{1}{\pi} \int_{\Sigma(t)} \mu(\mathbf{x}') \left[\frac{\partial \ln |\mathbf{x} - \mathbf{x}'|}{\partial \mathbf{n}(\mathbf{x}')} + 1 \right] \mathrm{d}s(\mathbf{x}') - 2J \ln |\mathbf{x}| = 2f(\mathbf{x}) \quad \text{for } \mathbf{x} \in \Sigma, \tag{6}$$

with

$$\int_{\Sigma(t)} \mu(\mathbf{x}') \, \mathrm{d}s(\mathbf{x}') = 0. \tag{7}$$

2.2. Behavior of the solution: linear analysis

We consider the nondimensionalized Hele–Shaw problem, in which the length scale is taken to be the equivalent initial radius of the bubble and the time scale is the characteristic surface tension relaxation time (i.e. $\tau = 12\mu R_0^3/(b^2\beta)$, where μ is the fluid viscosity, R_0 is the initial radius of the bubble, b is the gap between two plates, and β is the surface tension). The function $u(\mathbf{x})$ represents the nondimensional pressure field, and $f(\mathbf{x}) = -\kappa$ describes the nondimensional pressure jump across the interface $\Sigma(t)$ via the Laplace–Young condition. The normal velocity V at the interface is given by the pressure gradient

$$V(\mathbf{x}) = -\nabla u|_{\Sigma} \cdot \mathbf{n} \quad \text{for } \mathbf{x} \in \Sigma. \tag{8}$$

For a perturbed circular air bubble where the radius is perturbed by a Fourier mode k with amplitude $\delta_k(0)$ at $t = 0$, the linear evolution follows

$$r(\alpha, t) = R(t) + \delta_k(t)\cos k\alpha, \tag{9}$$

where $R(t)$ is the radius of the unperturbed circular bubble and $r(t)$ is the radius of the perturbed bubble. A classical linear stability analysis [6] gives the growth rate of underlying circle $R(t)$ as

$$R(t)\frac{\mathrm{d}R}{\mathrm{d}t} = J(t), \tag{10}$$

and the perturbation evolves as,

$$\left(\frac{\delta_k}{R}\right)^{-1}\frac{\mathrm{d}}{\mathrm{d}t}\left(\frac{\delta_k}{R}\right) = \frac{1}{R^2}(k-2)\left(J - \frac{C_k}{R}\right), \tag{11}$$

where the constant $C_k = k(k^2-1)/(k-2)$ arises due to the stabilizing effects of surface tension. Eq. (11) shows the perturbation grows (decays) for $J > C_k/R$ ($J < C_k/R$). In particular, when $J = C_k/R$, the perturbation is time independent the bubble evolves self-similarly (at the level of linear theory with a single mode perturbation). Hence, taking a constant flux or a flux that increases in time results in the growth of perturbations with larger and larger wavenumbers as R increases. This leads to the development of complex viscous fingering pattern, e.g. the Saffman–Taylor instability [5].

In this paper, $J(t)$ can be a general function of time, however, we focus on the following three types of fluxes $J = CR^p$, with C a nonzero constant and $p = 1$, 0 and -1:

- Linear flux with $p = 1$ (i.e. $J = CR(t)$). For a circular interface, it follows that $\mathrm{d}R/\mathrm{d}t = C$ and $R(t) \sim t$.
- Constant flux with $p = 0$ (i.e. $J = \mathrm{C}$). This flux gives the circular growth rate $\mathrm{d}R/\mathrm{d}t = C/R$ as $R(t) \sim t^{\frac{1}{2}}$. When R becomes large, the evolution slows down. Therefore, it is problematic to perform long-time simulations using this flux.
- Decreasing flux with $p = -1$ (i.e. $J = C/R(t)$). This flux gives a very slow growth rate $\mathrm{d}R/\mathrm{d}t = C/R^2$ and so $R(t) \sim t^{\frac{1}{3}}$. As suggested by the linear analysis, this flux may yield a nonlinear self-similar growth if $C \approx C_k$. In fact, as we show later, the very long-time evolution of bubbles under this injection flux yields compact, self-similarly growing shapes (for any choice of $C > 0$). Due to computational expense, it would be impractical to capture this very long-time behavior using simulation using the formulation in [9,39].

In the next section, we present the time and space rescaling scheme that allows us to overcome these practical limitations of computing large-size bubbles.

3. Time and space rescaling

We introduce the following spatial and temporal scaling

$$\mathbf{x} = \bar{R}(\bar{t})\bar{\mathbf{x}}(\bar{t}, \alpha), \tag{12}$$

$$\bar{t} = \int_0^t \frac{1}{\rho(t')}\,\mathrm{d}t', \tag{13}$$

where the scaling factor $\bar{R}(\bar{t}) = R(t(\bar{t}))$, $\bar{t}$ is the new time variable, and $\bar{\mathbf{x}}(\bar{t},\alpha)$ is the position vector of the scaled interface with α parameterizing the interface. The scaling function ρ is a function of t. Equivalently we may also define $\bar{\rho}(\bar{t}) = \rho(t(\bar{t}))$. Note that we can also write $\bar{J}(\bar{t}) = J(t(\bar{t}))$ in the scaled frame. The normal velocity in the scaled frame and the nonscaled (original) frame are related by

$$\bar{V}(\bar{t}) = \frac{\bar{\rho}}{\bar{R}} V(t(\bar{t})) - \frac{\bar{\mathbf{x}}\cdot\mathbf{n}}{\bar{R}} \frac{\mathrm{d}\bar{R}}{\mathrm{d}\bar{t}}. \tag{14}$$

The scaling $\bar{R}$ is chosen such that the area $\bar{A}$ enclosed by the scaled interface is constant in time, i.e. $\frac{\mathrm{d}\bar{A}}{\mathrm{d}\bar{t}} = 0$ and $\int_{\bar{\Sigma}} \bar{V}\,\mathrm{d}\bar{s} = 0$. Therefore, $\bar{R}$ can be found by integrating the normal velocity over the interface and dividing by 2π to get

$$\frac{\mathrm{d}\bar{R}(\bar{t})}{\mathrm{d}\bar{t}} = \frac{\pi\bar{J}\bar{\rho}}{\bar{A}\bar{R}}. \tag{15}$$

To achieve exponential growth of $\bar{R}$ in the scaled frame, we choose $\bar{\rho} = \dfrac{\bar{R}^2\bar{A}}{\bar{J}\pi}$ following Eq. (15). Solving Eq. (15) yields the exponential growth of scaling factor $\bar{R}$,

$$R(t) = \bar{R}(\bar{t}) = \exp(\bar{t}). \tag{16}$$

In particular, taking the flux $\bar{J} = C\bar{R}^p$ with $p < 2$, Eq. (13) gives the relation

$$t = \frac{\bar{A}}{C\pi(2-p)}\left[\exp((2-p)\bar{t}) - 1\right]. \tag{17}$$

To evolve the interface in the scaled frame, we need to compute the normal velocity of the interface $\bar{\Sigma}$. To start, we first use Eqs. (12) and (13) to scale the integral equation (Eq. (6)) as

$$\bar{\mu}(\bar{\mathbf{x}}) - \frac{1}{\pi}\int_{\bar{\Sigma}(t)} \bar{\mu}(\bar{\mathbf{x}}')\left[\frac{\partial \ln|\bar{\mathbf{x}}-\bar{\mathbf{x}}'|}{\partial\mathbf{n}(\bar{\mathbf{x}}')} + \bar{R}(\bar{t})\right]\mathrm{d}\bar{s}(\bar{\mathbf{x}}') = 2\bar{\kappa} + 2\bar{R}\bar{J}(\ln(\bar{R}) + \ln|\bar{\mathbf{x}}|), \tag{18}$$

where $\bar{\mu} = \mu R(t(\bar{t})) = \mu\bar{R}(\bar{t})$. Eq. (18) is a 2nd kind Fredholm integral equation, and has a unique solution [40]. Once we solve the dipole density $\bar{\mu}$ in the scaled frame, the nondimensional normal velocity $\bar{V}(\bar{\mathbf{x}})$ in the scaled frame can be calculated by the Dirichlet–Neumann map [43],

$$\bar{V}(\bar{\mathbf{x}}) = -\frac{\bar{A}}{2\pi^2\bar{R}\bar{J}}\left[\int_{\bar{\Sigma}} \frac{\partial\bar{\mu}}{\partial\bar{s}'}\frac{(\mathbf{x}(\bar{s})-\mathbf{x}(\bar{s}'))^{\perp}\cdot\mathbf{n}(\bar{s})}{|\bar{\mathbf{x}}(\bar{s})-\bar{\mathbf{x}}(\bar{s}')|^2}\,\mathrm{d}\bar{s}' + 2\pi\bar{R}\bar{J}\frac{\bar{\mathbf{x}}\cdot\mathbf{n}}{|\bar{\mathbf{x}}|^2}\right] - \bar{\mathbf{x}}\cdot\mathbf{n}, \tag{19}$$

where $\bar{\mathbf{x}}^{\perp} = (\bar{y}, -\bar{x})$. Then we can evolve the interface in the scaled frame through

$$\frac{\mathrm{d}\bar{\mathbf{x}}(\bar{t},\alpha)}{\mathrm{d}\bar{t}}\cdot\mathbf{n} = \bar{V}(\bar{t},\alpha). \tag{20}$$

To evolve the interface numerically, Eqs. (18) and (19) are discretized in space using spectrally accurate discretizations [9,33]. The integrals in Eq. (18) and (19) are evaluated using the fast multipole method [41]. The discrete system of Eq. (18) is solved efficiently using GMRES [42]. Because Eq. (18) is well-conditioned, no preconditioner is needed. Once the solution to the integral equation is obtained, the Dirichlet–Neumann map [43] is used to determine the normal velocity of the interface via Eq. (19) in the scaled frame. We then evolve the interface in the scaled frame using a second order accurate nonstiff updating scheme in time and the equal arclength parameterization [9,33].

4. Results and discussions

4.1. Convergence test

In this section, we test the convergence of the rescaling scheme. We confirm the numerical accuracy by considering an air bubble expanding into Hele–Shaw cell over very long times so that $\bar{R}(\bar{t})/\bar{R}(0)$ is large. We take an interface with initial shape, $(\bar{x}(\alpha,0),\bar{y}(\alpha,0)) = \bar{r}(\alpha,0)(\cos\alpha,\sin\alpha)$ where $\bar{r}(\alpha,0) = 1.0 + 0.1(\sin 2\alpha + \cos 3\alpha)$. This is the same initial data as used in [9,39]. In this calculation, we set the number of mesh points to be

$N = 32{,}768$ along the interface for the temporal resolution study. We also set the injection flux to be a constant in time $\bar{J}(\bar{t}) = J(t(\bar{t})) = 1.0$. We choose the initial area $\bar{A}(\bar{t} = 0)$ to be exact, and we compare the resulting area $\bar{A}(\bar{t})$ up to $\bar{t} = \bar{T} = 3.32$ (nonscaled time $T = 350$ which is the same scale used in [9,39]). We use time-steps $\Delta\bar{t} = 2.0\text{E} - 4$, $\Delta\bar{t} = 1.0\text{E} - 4$, and $\Delta\bar{t} = 0.5\text{E} - 4$. The error is measured in terms of the area difference, i.e. $|A(\bar{0}) - \bar{A}(\bar{t} = 3.32)|$. Fig. 1a shows the base 10 logarithm of the temporal error plotted versus scaling factor $R(t) = \bar{R}(\bar{t}(t))$. The distance between the curves uniformly decreases by a factor of 0.6, and this confirms the second order accuracy. The morphologies of the interfaces corresponding to different temporal resolutions at $\bar{T} = 3.32$ are shown as an inset. The resulting morphologies look almost identical, though the overall morphology takes a quite complex pattern. For $\Delta\bar{t} = 0.5\text{E} - 4$, the computation takes about 7 days on a computer with CPU 2.2 GHz Pentium 4 running Linux; for $\Delta\bar{t} = 1.0\text{E} - 4$, the simulation takes about 5 days; and for $\Delta\bar{t} = 2.0\text{E} - 4$, the simulation only takes about 3 days. Note that this computation goes far beyond the simulation originally shown in [9] where 50 days were required to perform a simulation with $T = 50$, and is close to the simulation by Fast and Shelley [39] where 50 days were required to reach $T = 500$.

We next test the resolution in space. We compare the shapes for $N = 8192$, 16,384, 32,768 and 65,536 mesh points along the interface. We set the injection flux $\bar{J} = 1.0$. For all computations, we choose $\Delta\bar{t} = 1.0\text{E} - 4$. The error is again measured as $|\bar{A}(0) - \bar{A}(\bar{t})|$. Fig. 1b shows the base 10 logarithm of the space error plotted versus scaling factor $R(t)$. At point A identified by a small circle at $R(t) \approx 10$ with $\bar{T} = 2.4$ in the scaled frame and $T = 55$ in the original frame. Note also the run with $N = 8192$ fails just after point A because more points are needed to resolve the interface. The computed area $\bar{A}$ for $N = 8192$ has 10 digits of accuracy when compared with the other runs using higher resolution. This is close to the GMRES tolerance 10^{-12}. Analogous results are obtained at point B with $R(t) = \bar{R}(\bar{t}) \approx 19$ ($\bar{T} = 2.96$ and $T = 170$) for $N = 16{,}384$, and at point C with $R(t) = \bar{R}(\bar{t}) \approx 42$ ($\bar{T} = 3.74$ and $T = 860$) for $N = 32{,}768$. If the resolution is increased to $N = 65{,}536$, we can run the simulation up to $R(t) \approx 68$ ($\bar{T} = 4.26$ and $T = 2300$) which will be analyzed further in the next section. This bubble is approximately four times larger than the one presented in [39] by Fast and Shelley, and takes less than half the computation time using a higher resolution. The corresponding morphologies for these three simulations are shown in Fig. 1c–e, respectively. At points A, B and C, the morphologies computed using different resolutions nearly overlap and the differences are indistinguishable to graphical resolution.

4.2. Very long-time simulations

As we demonstrated in the previous section, the rescaling scheme significantly reduces the computation time, and enables one to accurately simulate the long-time dynamics of moving interfaces. In this section,

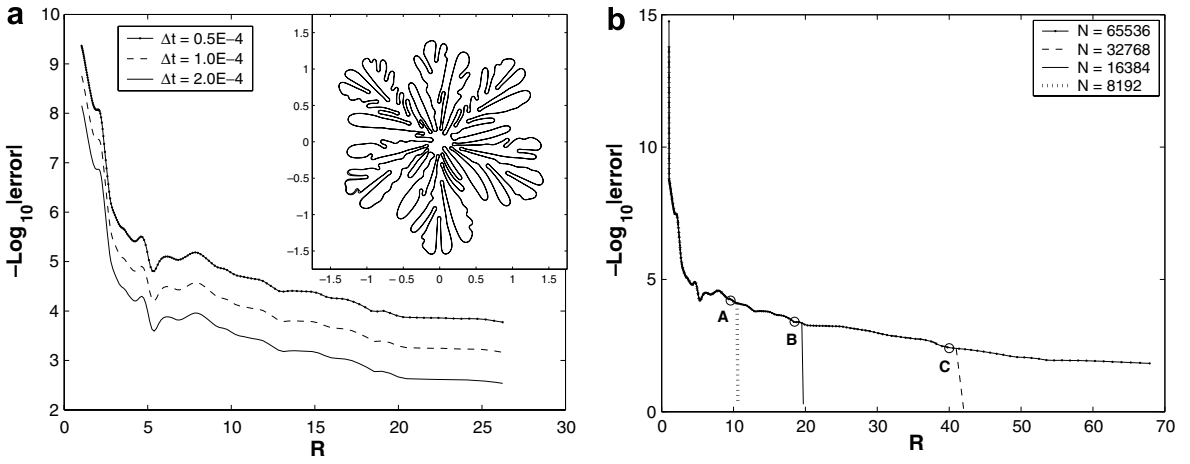

Fig. 1a and b. The convergence study of the rescaling scheme. The initial shape is chosen to be $(\bar{x}(\alpha, 0), \bar{y}(\alpha, 0)) = \bar{r}(\alpha, 0)(\cos\alpha, \sin\alpha)$ where $\bar{r}(\alpha, 0) = 1.0 + 0.1(\sin 2\alpha + \cos 3\alpha)$. (a) Shows the second order convergence in time. Associated morphologies at scaled time $\bar{T} = 3.32$ (nonscaled time $T = 350$) are shown in the inset. (b) Shows the spatial resolution study. The time-step is set to be $\Delta t = 1\text{E} - 4$.

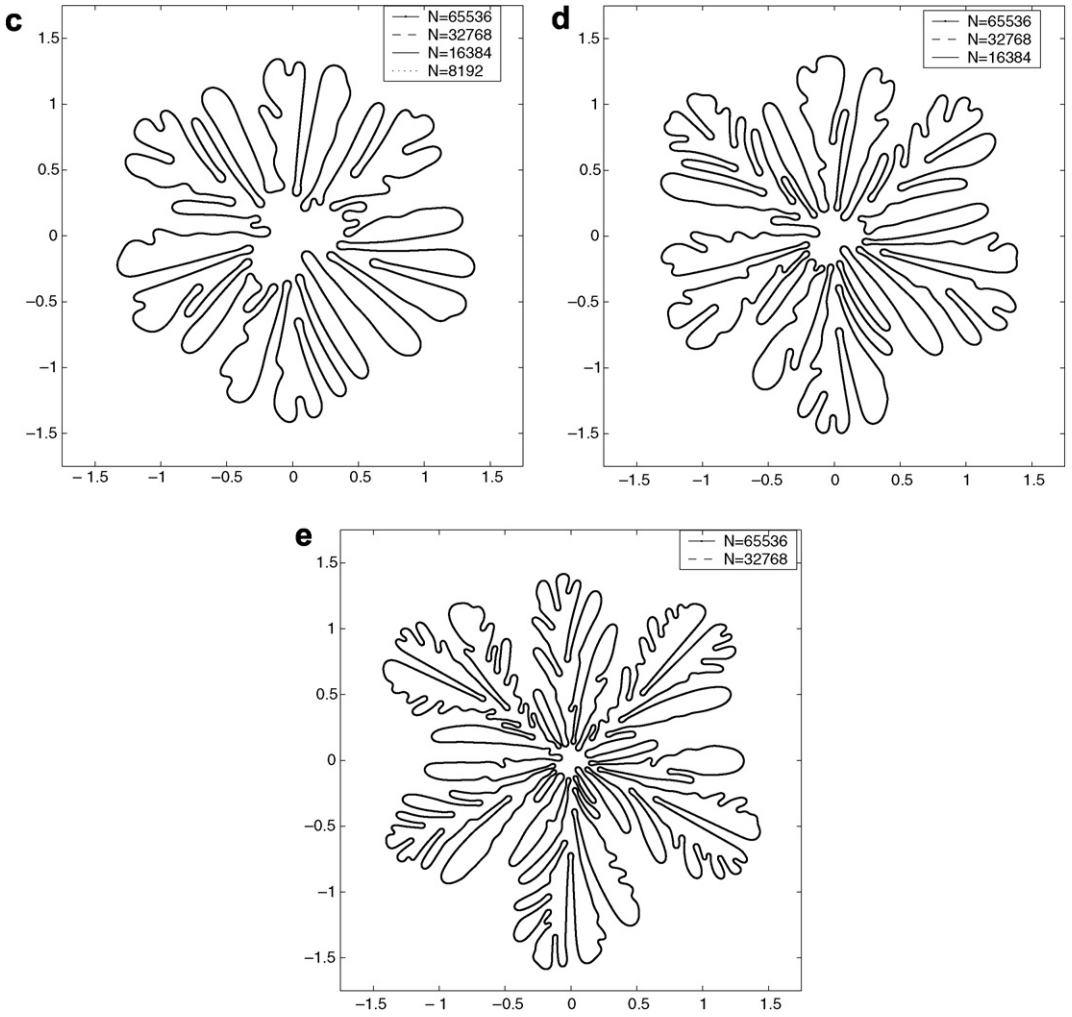

Fig. 1c, d and e. Show the detailed morphologies at points A, B and C (marked in Fig. 1b) for different spatial resolutions.

we perform very long-time simulations for the following three fluxes: $\bar{J}_1(\bar{t}) = \bar{R}(\bar{t})$ (i.e. $J_1(t) = R(t)$), $\bar{J}_2(\bar{t}) = 1.0$ (i.e. $J_2(t) = 1.0$) and $\bar{J}_3(\bar{t}) = 48/\bar{R}(\bar{t})$ (i.e. $J_3(t) = 48/R(t)$). The initial shape is chosen to be $(\bar{x}(\alpha,0), \bar{y}(\alpha,0)) = \bar{r}(\alpha,0)(\cos\alpha, \sin\alpha)$ where $\bar{r}(\alpha,0) = 1.0 + 0.1(\sin 2\alpha + \cos 3\alpha)$. We then measure the complexity of the interface by analyzing the relation between area $A(t)$ and arclength $L(t)$ in the nonscaled frame. For example, for a compact interface, $A(t) \sim L(t)^2$. However, when significant fingering is present, the overall morphology is fractal-like [44], and the arclength $L(t)$ grows much faster than $A(t)$, i.e. $A(t) \sim L(t)^{\gamma}$ with $\gamma < 2$. In the following figures, both $A(t)$ and $L(t)$ are presented in the nonscaled frame with $L(t)$ scaled by 2π, i.e. $A(t) = \bar{R}^2\bar{A}$ and $L(t) = \bar{R}\bar{L}/2\pi$.

4.2.1. Linear flux: $\bar{J}_1(\bar{t}) = \bar{R}(\bar{t})$

Fig. 2a shows a long-time simulation for applied flux $\bar{J}_1(\bar{t}) = \bar{R}(\bar{t})$, i.e. the flux increases linearly with the bubble size. Using the same initial condition as in Fig. 1 (also given explicitly above), we start this computation using $N = 65{,}536$ mesh points, and time-step is set to be $\Delta\bar{t} = 1.0\text{E}-4$. The computation ended at $\bar{T} = 2.2$ ($T = 8.2$ in the nonscaled frame) with $\bar{R} = 9$ because more points are needed to resolve the highly complex interface beyond this point. For completeness, we have reproduced this simulation using the same algorithm as in [39] and found the simulation also broke down at this point. At the very early growth stages, the

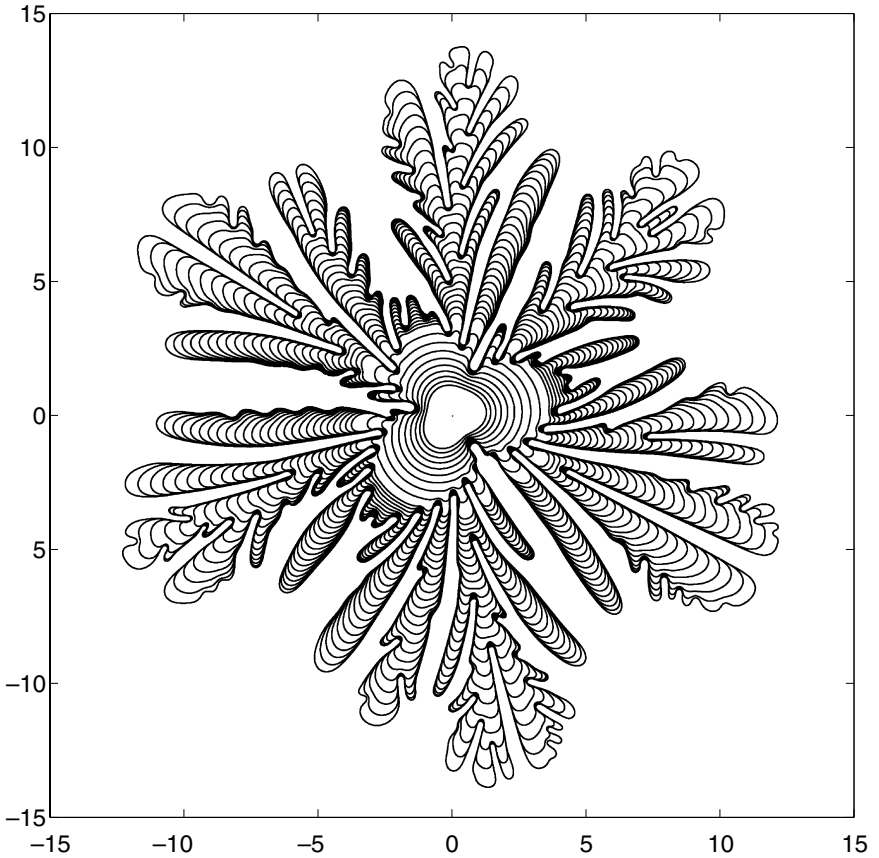

Fig. 2a. Shows the long-time simulation for flux $\bar{J}(\bar{t}) = \bar{R}(\bar{t})$ (i.e. $J(t) = R(t)$). The initial shape is chosen to be $(\bar{x}(\alpha,0),\bar{y}(\alpha,0)) = \bar{r}(\alpha,0)(\cos\alpha,\sin\alpha)$ where $\bar{r}(\alpha,0) = 1.0 + 0.1(\sin 2\alpha + \cos 3\alpha)$. Time-step $\Delta\bar{t} = 1\mathrm{E}-4$. The resolution $N = 65{,}636$ is used throughout the calculation. The calculation is performed in the scaled frame and then mapped back onto the nonscaled frame to compute $A(t)$ and $L(t)$. (a) Shows the detailed evolution sequences. we show outputs from $\bar{T} = 0$ to $\bar{T} = 1.2$ every 1200 time-steps; from $\bar{T} = 1.2$ to $\bar{T} = 2.2$ every 400 time-steps.

shape is essentially compact, subsequently few viscous fingers develop on the three main branches. At later times, the morphology experiences successive tip-splitting events and rapidly develops a highly ramified pattern.

In Fig. 2b the area $A(t)$ is shown versus arclength $L(t)$ for simulations using three different initial data. For the initial data considered in Fig. 2a (solid dotted curve labeled mode mixture 2, 3), there are two transitions connecting three roughly linear segments with different slopes marked along the $A(t)$ versus $L(t)$ curve, and five typical morphologies are shown as insets to demonstrate the development of the bubble. When $A(t)$ is small (at the early stages of growth), the shape remains compact (as shown by the first two insets) and $A \sim L^{1.95}$. As the area increases, the first transition occurs at $A = 15$ and $L = 2.7$ ($\bar{R} = 2.2$) and $A \sim L^{0.55}$. This regime is characterized by numerous tip-splitting events that dramatically increase the number of fingers. As a result, complex shapes develop as shown in Fig. 2a and in the insets. The second transition from $A \sim L^{0.55}$ to $A \sim L^{1.05}$ occurs around $A = 75$ and $L = 28$ ($\bar{R} = 5$). This scaling indicates that the growth rate of the arclength decreases and suggests fewer tip-splitting events occur in this region. The values of the parameter γ marked in the graph correspond to the initial data considered in Fig. 2a.

Two similar tests were performed using different initial data. One initial data contains many modes (solid curve labeled as mode mixture 2, 3, 4, 5, 7, 8, 11), and the other contains only a single mode 4 (dashed curve). At early growth stages, the values of the parameter γ depend sensitively on the initial data when the interface remains compact; however, when the interfaces evolve into highly ramified fingering patterns, the scaling property is independent of the initial data and $\gamma \approx 1.0$.

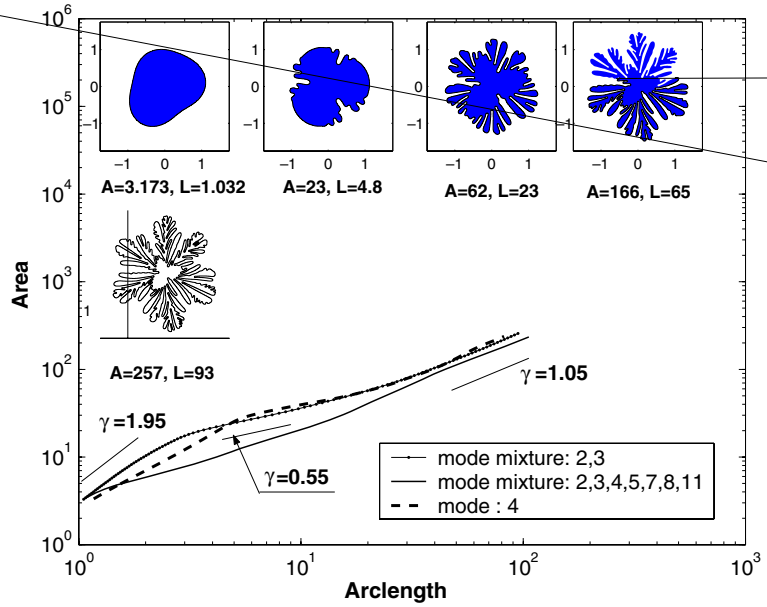

Fig. 2b. Shows the relation between $A(t)$ and $L(t)$ starting from three different mode mixtures. The flux is set to be $J(t) = R(t)$. The insets and the parameter γ marked along the curve correspond to the initial shape with modes 2 and 3 as in Fig. 2a. The shape gives γ where $A(t) \sim L(t)^{\gamma}$.

4.2.2. Constant flux $\bar{J}_2(\bar{t}) = 1.0$

In Fig. 2c, we present a simulation of ramified viscous fingering patterning using $\bar{J}_2(\bar{t}) = 1.0$. The initial condition and parameters used in the calculation are the same as in [9,39] and Fig. 1. This simulation ran about 3 weeks and ended at $\bar{T} = 4.26$ ($T = 2300$ in the nonscaled frame) with $\bar{R}(\bar{t}) = 68$. Higher spatial resolution is needed to run the simulation beyond this point. Comparing the computation cost with [39] , our simulation ran 4 times longer and used less than half the computation time, though we used a higher resolution ($N = 65{,}536$) throughout the entire simulation. In particular, using the rescaling scheme, it took 6 days to reproduce the results that took 50 days to compute in [39]. Comparing the morphology with that presented in [39], our simulation shows a much more pronounced viscous fingering pattern.

In Fig. 2d, the area $A(t)$ is shown versus arclength $L(t)$ for simulations using three different initial data. For the initial data considered in Fig. 2c (solid dotted curve labeled mode mixture 2,3), there are three transitions in the $A(t)$ versus $L(t)$ curve (marked by the three short lines with different slopes,) are observed to occur during the simulation. The first was observed by Hou et al. [9], and the second was captured by Fast and Shelley [39]. We identify the third transition where tip-splitting events seemingly accelerate again. Six typical morphologies are shown as insets. Comparing Fig. 2d and 2b, the insets show that for a given bubble area, the shape for $\bar{J} = \bar{R}$ is more complex. This is also confirmed by the smaller scaling parameter γ for $\bar{J} = \bar{R}$.

Additional simulations were also performed using the same initial data as in Fig. 2b. As in the case $J(t) = R(t)$, the case with $J(t) = 1.0$ reveals that at early growth stages, the scaling depends on the initial shape. However, when the interfaces evolves into highly ramified fingering patterns, the scaling is initial data independent and $\gamma \approx 1.5$.

4.2.3. Time decreasing flux $\bar{J}_3(\bar{t}) = 48/\bar{R}$

Fig. 2e shows a simulation for a time decreasing flux $\bar{J}_3(\bar{t}) = 48.0/\bar{R}(\bar{t})$. We use $N = 2048$ mesh points in the calculation. The calculation ran about three hours and ended at $\bar{T} = 0.5$ ($T = 6.4\text{E}28$ in the nonscaled frame) with $\bar{R}(\bar{t}) = R(t) = 2.1\text{E}10$. The results of this simulation are dramatically different from the previous two cases. During the evolution, the morphology of the bubble remains compact, and there is only one tip-splitting

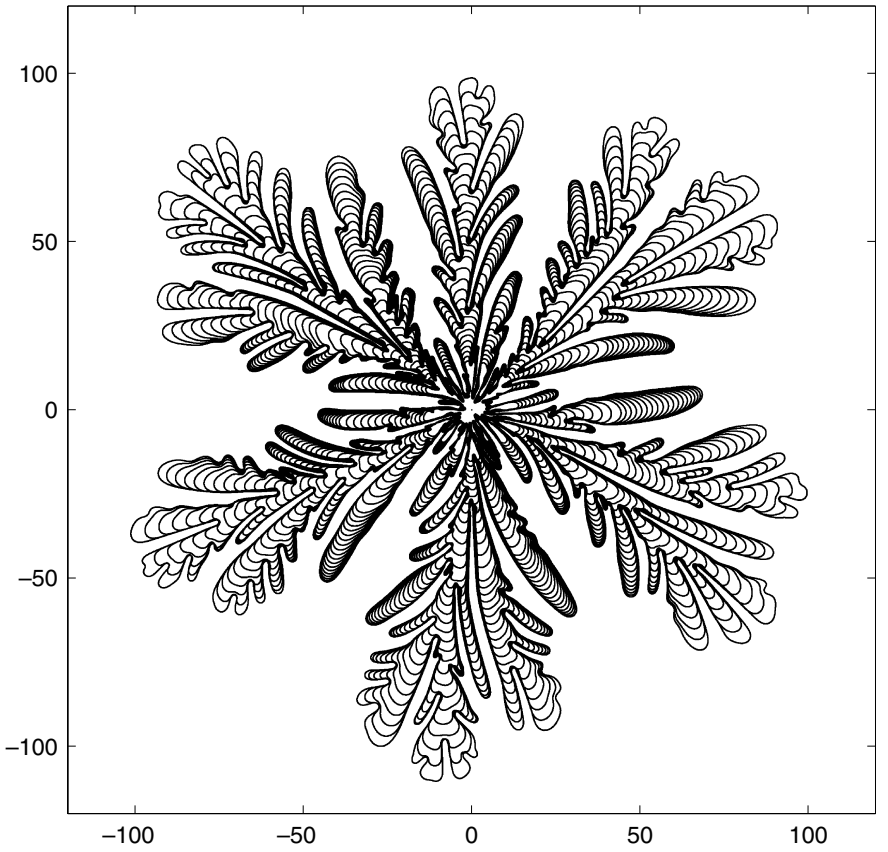

Fig. 2c. Shows the detailed evolution sequences for flux $\bar{J}(\bar{t}) = J(t) = 1.0$. Due to the dense evolution sequence, we show outputs from $\bar{T} = 2.4$ to $\bar{T} = 3.6$ every 800 time-steps; from $\bar{T} = 3.6$ to $\bar{T} = 4.26$ every 400 time-steps. Note that $\bar{T} = 4.26$ is equivalent to $T = 2300$ in the nonscaled frame. It took about 3 weeks to compute the above bubble on a computer with CPU 2.2 GHz Pentium 4 running Linux.

event. Consequently, the $A(t)$ versus $L(t)$ curve (shown in Fig. 2f) is almost a straight line with a slope slightly less than 2 at the early growth stages, and tending to 2 when $A(t)$ is large.

Fig. 2g shows the shape factor δ/R versus the scaling factor $\bar{R}(\bar{t}) = R(t)$. The shape factor is defined as

$$\delta/R = \max ||\bar{\mathbf{x}}|/\bar{R}_{\text{eff}} - 1|, \tag{21}$$

where $\bar{\mathbf{x}}$ is the position vector from the centroid of the shape to the interface and $\bar{R}_{\text{eff}} = \sqrt{\dfrac{\bar{A}}{\pi}}$ is the effective radius of the bubble in the scaled frame. As shown in Fig. 2g, shape perturbations grows rapidly at early times. However, at long times nonlinear stabilization occurs and leads to the existence of noncircular limiting shapes. That is, the morphology of the nonlinearly evolving bubble tend to the limiting shape that evolves self-similarly. Moreover, the limiting shape is universal in the sense it is independent of the initial shape and only depends on the applied flux. To see this, in Fig. 2g, we consider computations from three different initial conditions and use the same flux. All the simulations are found to converge to the same universal shape. The limiting universal shape has a 4-fold symmetry. This is because under the specific injection flux $\bar{J}_3$, mode 4 is the fastest growing among all modes. Though in certain cases as shown in Fig. 2g, mode 4 may not be present initially, nonlinear interactions among modes create mode 4, which then grows the fastest and dominates the overall shape. A dimensional analysis shows that the time scales for growth and stabilization balance at long times (e.g. see [46] in the context of crystal growth). Analogous universal limiting shapes were previously observed in the context of crystal growth, see [37,38]. We are currently investigating this phenomena in a joint theoretical/experimental study of bubble evolution in a Hele–Shaw cell [45].

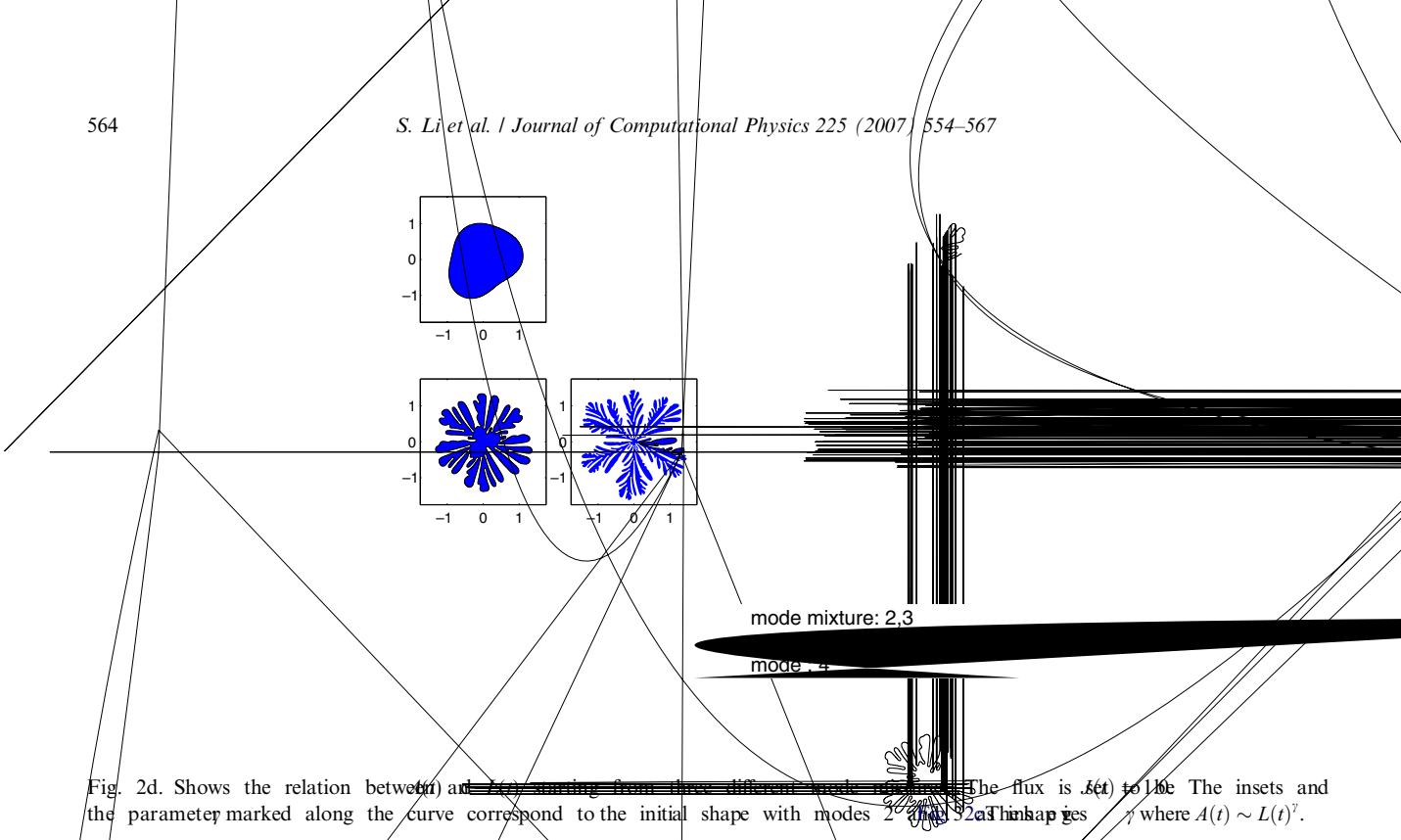

Fig. 2d. Shows the relation between $A(t)$ and $L(t)$ starting from three different initial conditions. The flux is set to be $J(t) = 1$. The insets and the parameter marked along the curve correspond to the initial shape with modes 2, 3 and 4 and the shapes at the corresponding times where $A(t) \sim L(t)^{\gamma}$.

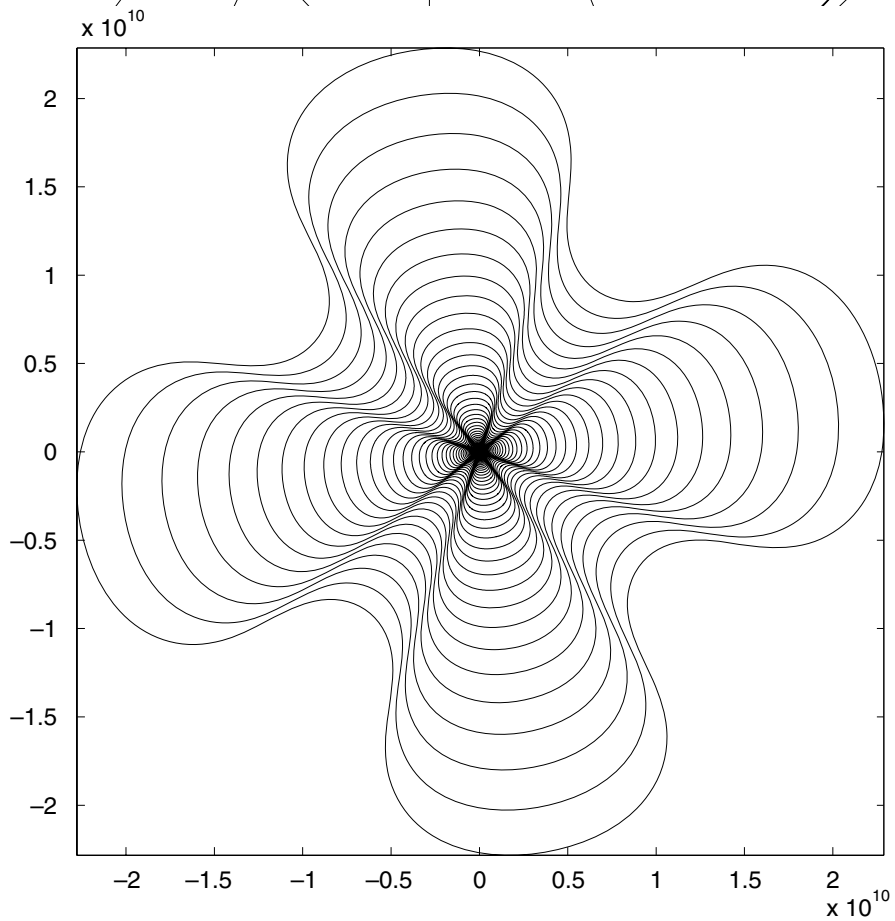

Fig. 2e. Shows the self-similar evolution sequences (at long times) for flux $J(t) = \dfrac{48}{R(t)}$. The spatial resolution is $N = 2048$.

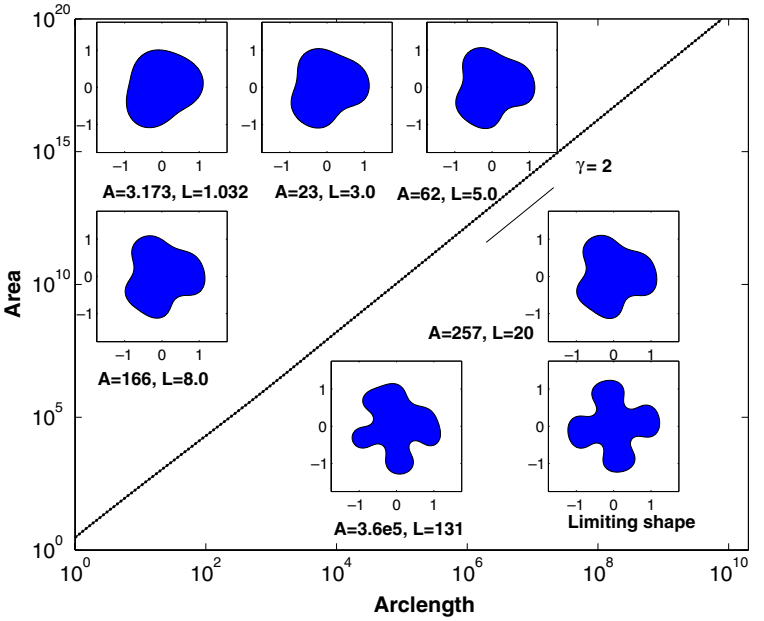

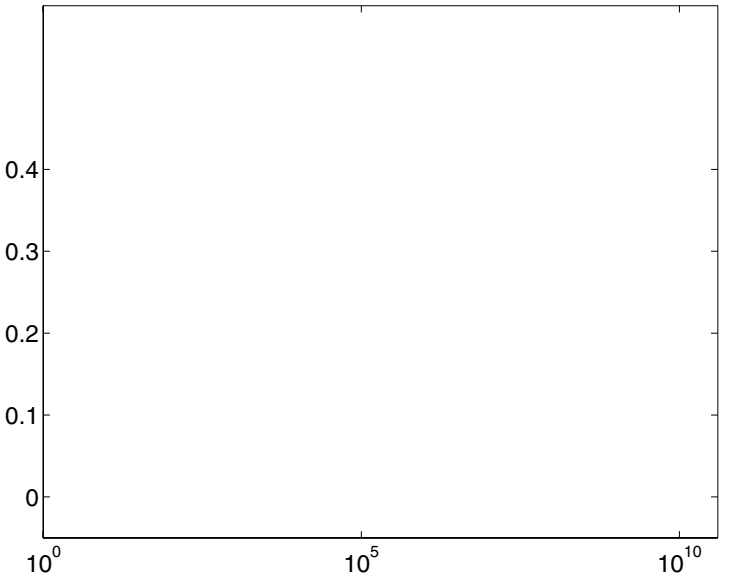

5. Conclusions

In this paper, we develop a rescaling scheme and simulated the growth of very large bubbles in a Hele–Shaw cell. Time is scaled such that the bubble size grows exponentially fast in the new time scale, and space is scaled such that the area is constant in the new frame. The scheme overcomes slow growth mechanisms while maintaining the original physics. By reducing the computation time, this rescaling scheme significantly improves the performance of the boundary integral method originally developed by Hou, Lowengrub and Shelley [9], and enables one to accurately simulate the very long-time dynamics of moving interfaces. We then present the largest and most pronounced viscous fingering simulations to date.

We investigate the evolution of interface morphologies to very long times under several injection fluxes $J \propto R(t)^p$ with $p = 1$, 0 and -1, examine the morphologies and measure the bubble complexity in terms of a relation between area $A(t)$ and arclength $L(t)$, i.e. $A(t) \sim L(t)^\gamma$. The relation reflects the underlying physics: when $\gamma < 2$, the destabilizing driving force (flux) dominates the evolution and leads to complex fractal-like shapes, the smaller the power, the more complex the shape; when $\gamma = 2$, the stabilizing force (surface tension) and destabilizing factor balance, and leads to the development of compact morphologies. When $J \propto R$, the interface rapidly evolves into a highly ramified fingering pattern and $\gamma \approx 1$ at long times; when $J \propto 1$, the interface also develops ramified fingering pattern and $\gamma \approx 1.5$ at long times; when $J \propto 1/R$, shape perturbations grows rapidly at early times. However, at long times nonlinear stabilization occurs and leads to the existence of noncircular limiting shapes, i.e. the morphologies of a growing bubble tend to noncircular limiting shapes that evolve self-similarly and $\gamma \approx 2$.

Though we focus our formulation and study on a two dimensional problem, the formulation can be extended to three dimensions. For example, Cristini and Lowengrub developed a similar approach to study a 3D crystal growth problem, in which a single layer potential theory was used [46].

Finally, the rescaling scheme can be applied more generally in interface problems containing additional physical processes such as the effect of surface energy anisotropy (e.g. [47]).

Acknowledgments

The authors thank Prof. M. Shelley and P. Fast for stimulating discussions and for sending a version of the HLS94 code [9] with improved data structures. The authors thank the National Science Foundation (Division of Mathematical Science) and the University of Minnesota Office of Sponsored Projects for partial support. S. Li thanks Yubao Zhen for technical discussions. The authors also acknowledge the generous computing resources from the Network and Academic Computing Services (NACS) at University of California at Irvine (UCI), and the hospitality of Biomedical Engineering Department at UCI.

References

[1] J.S. Langer, Instability and pattern formation in crystal growth, Reviews of Modern Physics 52 (1) (1980).
[2] Eshel Ben-Jacob, Peter Garik, The formation of patterns in non-equilibrium growth, Nature 343 (1990) 523.
[3] E. Ben-Jacob, G. Deutscher, P. Garik, Nigel D. Goldenfeld, Y. Lareah, Formation of a dense branching morphology in interfacial growth, Phys. Rev. Lett. 57 (1986) 1903–1906.
[4] H.S. Hele–Shaw, Nature 58 (1898) 34–36.
[5] P.G. Saffman, G.I. Taylor, The penetration of a fluid into a porous medium or a Hele–Shaw cell containing a more viscous fluid, Proc. R. Soc. London A 245 (1958) 312.
[6] W.W. Mullins, R.F. Sekerka, Morphological stability of a particle growing by diffusion or heat flow, J. Appl. Phys. 34 (1963) 323–329.
[7] C. Pozrikidis, Interfacial dynamics for stokes flow, J. Comput. Phys. 169 (2001) 250.
[8] C. Pozrikidis, Boundary Integral and Singularity Methods for Linearized Viscous Flow, Cambridge University Press, Cambridge, 1992.
[9] T.Y. Hou, J.S. Lowengrub, M.J. Shelley, Removing the stiffness from interfacial flows with surface tension, J. Comput. Phys. 114 (1994) 312–338.
[10] S. Osher, J.A. Sethian, Front propagating with curvature-dependent speed: algorithms based on Hamilton–Jacobi formulations, J. Comput. Phys. 79 (1988) 12.
[11] S. Osher, R.P. Fedkiw, Level set method: an overview and some recent results, J. Comput. Phys. 169 (2001) 463.
[12] J. Sethian, Level set methods, Cambridge University Press, Cambridge, 1996.
[13] J. Sethian, P. Smereka, Level set methods for fluid interfaces, Ann. Rev. Fluid Mech. 35 (2003) 341.
[14] C.W. Hirt, B.D. Nichols, Volume of fluid (VOF) method for the dynamics of free boundaries, J. Comput. Phys. 39 (1981) 201.
[15] R. Scardovelli, S. Zaleski, Direct numerical simulation of free-surface and interfacial flow, Ann. Rev. Fluid Mech. 31 (1999) 567.
[16] J. Glimm, M. Graham, J. Grove, X. Li, T. Smith, D. Tan, F. Tangerman, Q. Zhang, Front tracking in two and three dimensions, Comput. Math. Appl. 35 (1998) 1.
[17] G. Tryggvason, B. Buner, A. Esmaeeli, D. Juric, N. Al-Rawahi, W. Tauber, J. Han, S. Nas, Y. Jan, A front-tracking method for the computation of multiphase flow, J. Comput. Phys. 169 (2001) 708.
[18] R.J. Leveque, Z. Li, Immersed interface methods for stokes flow with elastic boundaries or surface tension, SIAM J. Sci. Comput. 18 (1997) 709.
[19] Z. Li, Immersed interface methods for moving interface problems, Numer. Algorithms 14 (1997) 269–293.

[20] S.L. Wang, R.F. Sekerka, A.A. Wheeler, B.T. Murray, S.R. Coriell, R.J. Braun, G.B. McFadden, Thermodynamically-consistent phase-field models for solidification, Physica D 69 (1993) 189.
[21] J. Kim, J. Lowengrub, Interfaces and Multicomponent Fluids, to appear in Encyclopedia of Mathematical Physics, Elsevier, 2006.
[22] Pengtao Yue, Chunfeng Zhou, James J. Feng, Carl F. Ollivier-Gooch, Howard H. Hu, Phase-field simulations of interfacial dynamics in viscoelastic fluids using finite elements with adaptive meshing, J. Comput. Phys. 219 (2006) 47–67.
[23] J.S. Langer, in: G. Grinstein, G. Mazenko (Eds.), In Directions in Condensed Matter Physics, World Scientific, Singapore, 1986.
[24] T.Y. Hou, Z. Li, S. Osher, H. Zhao, A hybrid method for moving interface problems with application to the Hele–Shaw flow, J. Comput. Phys. 134 (1997) 236–252.
[25] H.D. Ceniceros, The effects of surfactants on the formation and evolution of capillary waves, Phys. Fluids 15 (2003) 245.
[26] D. Enright, R. Fedkiw, J. Ferziger, I. Mitchell, A hybrid particle level set method for improved interface capturing, J. Comput. Phys. 183 (2002) 83.
[27] X. Yang, A.J. James, J. Lowengrub, X. Zheng, V. Cristini, An adaptive coupled level-set/volume-of-fluid interface capturing method for unstructured triangular grids, J. Comput. Phys. 217 (2006) 364–394.
[28] T.Y. Hou, J.S. Lowengrub, M.S. Shelley, The long time motion of vortex sheets with surface tension, Phys. Fluids 9 (1997) 1933–1954.
[29] M. Ben Amar, D. Bonn, Fingering instability in adhesive failure, Physica D 209 (2005) 1–16.
[30] M. Shelley, F. Tian, K. Wlodarski, Hele–Shaw flow and pattern formation in a time-dependent gap, Nonlinearity 10 (1997) 1471–1495.
[31] A. Tatulchenkov, A. Cebers, Complex bubble dynamics in a vertical Hele–Shaw cell, Phys. Fluids 17 (2005) 107103.
[32] J.A. Miranda, E. Alvarez-Lacalle, Viscosity contrast effects on fingering formation in rotating Hele–Shaw flows, Phys. Rev. E 72 (2005) 026306.
[33] T.Y. Hou, J.S. Lowengrub, M.J. Shelley, Boundary integral methods for multicomponent fluids and multiphase materials, J. Comput. Phys. 169 (2) (2001) 302–362.
[34] H.J. Jou, P. Leo, J. Lowengrub, Microstructural evolution in inhomogeneous elastic media, J. Comput. Phys. 131 (1997) 109–148.
[35] V. Cristini, J. Lowengrub, Q. Nie, Nonlinear simulation of tumor growth, J. Math. Biol. 46 (3) (2003) 191–224.
[36] S. Li, J. Lowengrub, P. Leo, V. Cristini, Nonlinear theory of self-similar crystal growth and melting, J. Cryst. Growth 267 (2004) 703–713.
[37] S. Li, J. Lowengrub, P. Leo, V. Cristini, Nonlinear stability analysis of self-similar crystal growth: control of the Mullins–Sekerka instability, J. Cryst. Growth 277 (2005) 578–592.
[38] S. Li, J. Lowengrub, P. Leo, Nonlinear morphological control of growing crystals, Physica D 208 (2005) 209–219.
[39] P. Fast, M. Shelley, Moore's law and the Saffman–Taylor instability, J. Comput. Phys. 212 (2006) 1–5.
[40] S.G. Mikhlin, Integral Equations and their Applications to Certain Problems in Mechanics, Mathematical Physics and Technology, Pergamon, New York, 1957.
[41] L. Greengard, V.I. Rokhlin, A fast algorithm for particles summations, J. Comput. Phys. 73 (1987) 325–348.
[42] Y. Saad, M.H. Schultz, GMRES: a generalized minimal residual algorithm for solving nonsymmetric linear systems, SIAM J. Sci. Stat. Comput. 7 (1986) 856–869.
[43] A. Greenbaum, L. Greegard, G.B. Mcfadden, Laplace's equation and the Dirichlet–Neumann map in multiply connected domains, J. Comput. Phys. 105 (1993) 267–278.
[44] P. Meakin, Fractal, Scaling and Growth far from Equilibrium", Cambridge University Press, Cambridge, 1998.
[45] S. Li, J. Lowengrub, J. Fontana, P. Palffy-Muhoray, P. Leo, in preparation.
[46] V. Cristini, J. Lowengrub, Three-dimensional crystal growth. II: nonlinear simulation and control of the Mullins–Sekerka instability, J. Cryst. Growth 266 (2004) 552–567.
[47] M.E. Glicksman, J.S. Lowengrub, S. Li, Non-monotone temperature boundary conditions in dendritic growth, in: C.A. Gandin, M. Bellet (Eds.), Proc. in Modelling of Casting, Welding and Adv. Solid. Processes XI, 2006, pp. 521–528.